CrystEngComm

Accepted Manuscript

ROYAL SOCIETY OF CHEMISTRY

www.rsc.org/crystengcomm

Graphic Abstract

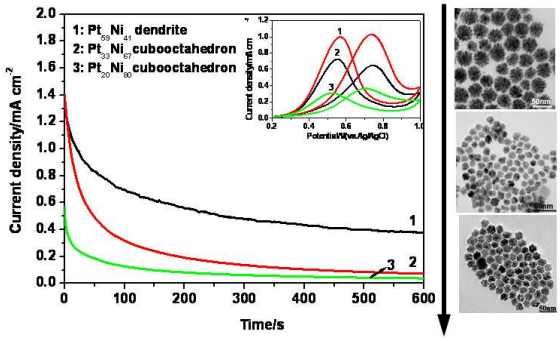

The composition and morphology evolution for Pt_xNi_{1-x} ($0 < x < 1$) nanoalloys was achieved by adjusting the growth kinetics. It was found the transformation processes were different under different temperature. The methanol oxidation reaction was chosen as the model reaction to evaluate the morphology- and composition-dependent electrocatalytic performance. It revealed that the dendrites exhibited the higher catalytic activity and better durability than the cuboctahedrons, which was illustrated from the viewpoint of the geometry and electronic structure.

Cite this: DOI: 10.1039/c0xx00000x

www.rsc.org/xxxxxx

ARTICLE TYPE

From Pt-rich Dendrites to Ni-rich Cuboctahedrons: the Composition and Morphology Evolution of Pt_xNi_{1-x} (0 < x < 1) Nanoalloys and Their Electrocatalytic Properties towards Methanol Oxidation

Dong-Feng Zhang,* Jian-Xin Kang, Ting-Wen Chen, Yan Zhang, Li-Li Wang, Jie Li, Lin Guo*

Received (in XXX, XXX) Xth XXXXXXXXX 20XX, Accepted Xth XXXXXXXXX 20XX
DOI: 10.1039/b000000x

In this paper, we report the composition and morphology evolution of Pt_xNi_{1-x} (0 < x < 1) nanoalloys from Pt-rich dendrites to Ni-rich cuboctahedrons. However, the transformation processes were different under different temperature. At 200 °C, the transformation was mainly completed through atomic addition, while it was contributed by both atomic addition and oriented attachment under 220 °C. The electrocatalytic performance evaluation towards methanol oxidation reaction (MOR) indicated the dendrites exhibited the higher catalytic activity and better durability relative to the cuboctahedrons. For the cuboctahedrons with different composition, the catalytic activity is mainly determined by the d-band position. It would provide new insight into the controlled synthesis of Pt-based bimetallic nanoalloys and advance the understanding of their catalytic behaviour.

1. Introduction

Improving the catalytic performance and reducing the usage of costly Pt electrocatalysts is still the major challenge for the commercialization of the fuel cell mainly including polymer electrolyte membrane fuel cell (PEMFC) and direct methanol fuel cell (DMFC). A promising approach to solve the problems is to design Pt-based bimetallic catalysts with rational geometric and electronic structures.[1-4] It has been well-established that the d-band position of a catalyst played a decisive role in determining the catalytic properties by modulating the adsorption energies of the reactants on the catalyst as well as their activation energies.[5-9] The d-band centre position is found not only dependent on the lattice strain and charge transfer between different metals but also closely related to the local coordination environment and surface atomic arrangement.[10-15] Therefore, alloying Pt with less expensive transition metals such as Fe, Co, Ni and their morphology control has great implication.

Since Stamenkovic and the collaborators in 2007 reported an over 10-fold enhancement in area specific activity for ORR of Pt_3Ni (111) relative to Pt (111) and 90-fold relative to the state-of-the-art Pt/C catalysts for PEMFC,[5] bimetallic Pt_xNi_{1-x} nanoalloys raised increasing concern as exciting electrocatalyst candidates. Besides very few reports involved in the surfactant-free solvothermal synthesis,[16-18] surfactant-directed synthesis is the most-often adopted strategy for the shape control of PtNi alloys.[19-28] For instance, Yang's and Fang's group recently reported the shape-selective synthesis of PtNi nanoparticles by carefully choosing different surfactants, reducing agents, solvents and introducing sequence of the precursor.[23-26] With oleylamine serving simultaneously as the solvent, reducing agent, and stabilizer, Prof. Lou and his collaborates reported the preparation of one-dimensional (1D) Pt-based nanomaterials.[27-29] However, the fundamental understanding of how the critical reaction parameters affect the composition and morphology has still remained largely unaddressed in the literature, which is the prerequisite to achieve a high-level control of Pt-based nanoalloys.

Generally, nanocrystals with well-defined shapes were considered to grow by atomic addition driven by the lowest surface energy, where the surface energies can be modulated by the facet-specific adsorbing of capping agents. However, in this paper, we report that the Ni-rich Pt_xNi_{1-x} nanocuboctahedrons were evolved from Pt-rich nanodendrites. The transformation process was different at different temperature range. At relative lower temperature, atomic addition played a key role, while oriented attachment and atomic addition were equally important at relative higher temperature range. It would provide new insight into the composition and morphology control of Pt-based bimetallic nanoalloys. The electrocatalytic activity of the Pt_xNi_{1-x} alloys with different composition and morphologies were investigated with methanol oxidation as the model reaction.

2. Experimental Section

2.1 Preparation of Pt_xNi_{1-x} nanoparticles

All the reagents used in this work were of analytical grade and used as received. In a typical synthesis, $H_2PtCl_6 \cdot 6H_2O$ (0.07 mmol in 0.3 mL of ethanol) and $Ni(acac)_2 \cdot 4H_2O$ (0.14 mmol), 1,2-Dodecanediol (5.0 mmol) were dissolved in a solution containing 8.0 mL oleylamine and 2.0 mL oleic acid. After stirring in water bath at 40 °C for 1h, the mixture was purged with Ar gas for 20min. It was first heated to 120 °C and evacuated for

10 min to remove the water vapour. Then, the temperature was raised to a given temperature at a rate of 10 $^{o}C \cdot min^{-1}$ and kept at that temperature for given times. After cooling to room temperature, the products were collected by centrifugation, and washed with ethanol and hexane alternately for several times. By keeping the aging temperature as 200 or 220 $^{\circ}C$ for 0 to 90 min, Pt_xNi_{1-x} nanoparticles of different shape and composition were obtained and the formation mechanism was studied.

2.2 Characterizations

Transmission electron microscopy (TEM) and High-resolution transmission electron microscopy (HRTEM) were employed to characterize the morphologies and structures of the products carried out at JEOL JEM-2100F with an accelerating voltage of 200 kV. Elemental distribution profiles were collected by energy dispersive X-ray spectrometer (EDAX) equipped within the JEOL JEM-2100F TEM. The structure of the products was characterized by the powder X-ray diffraction (XRD) using a Rigaku Rotaflex Dmax2200 diffractometer with Cu Kα radiation (λ = 1.5406 Å). X-Ray photoelectron spectroscopy (XPS) measurement was carried out on an Axis Ultra spectrometer at a pressure lower than 10-8 Torr with a standard Al Ka excitation source (1486.6 eV). The charging effect was corrected by adjusting the binding energy of the main C 1s peak to 284.6 eV.

2.3 Electrode preparation and electrochemical measurements

To prepare the working electrode, glassy carbon electrodes (Φ3mm) were polished to a mirror-finish prior to each experiment and served as substrates for the catalysts. An aliquot of 5.0 μL of 2 mg/mL as-synthesized nanocatalyst suspension in deionized water was dropped onto the glassy carbon electrode and dried in an incubator. Then, 7 μL of Nafion alcohol solution (0.25 wt %) were coated on the top of the dried catalyst layer and the electrode was dried in an incubator. Electrochemical measurements were performed using a CHI 660C electrochemical workstation (Chenhua, Shanghai) at room temperature (about 25 $^{\circ}C$). A Pt wire served as the counter electrode, and a Ag/AgCl electrode saturated with KCl solution was used as the reference electrode. The cyclic voltammetry (CV) measurements were carried out in the aqueous solution of 0.5 mol/L H_2SO_4 with/or without 1.0 mol/L CH_3OH for different purposes. Chronoamperometry measurements were performed under a potential of 0.7 V for 600 s in 0.5 mol/L H_2SO_4 solution containing 1.0 mol/L CH_3OH. All solutions were fully purged with Ar gas before the measurements. The electrode potential in this study is reported with respect to the reversible hydrogen electrode (RHE).

3. Results and discussions

We demonstrated here that Pt-Ni nanoalloys with different composition and different morphologies can be achieved by simply adjusting the reaction temperature via a solvothermal route. Fixing the reaction time as 1 h, when the reaction was carried out at 200 °C, the products exhibited as well-dispersed dendritic nanostructures with formation yield as high as 100%. The size of the dendrites ranged from 24 to 42 nm with an average diameter of 28 nm (Figure 1a). The high-resolution transmission electron microscope (HRTEM) image of an individual nanodendrite indicated the branches were in various directions with width of ~4 nm (Figure 1b). The lattice fringes were coherently extended across over several branches. The clearly observable domain boundaries indicated the individual dendritic structure was of polycrystalline nature, which were further confirmed by the selected area electron diffraction (SAED) characterization. As shown in the top-right inset of Figure 1a, the SAED pattern of the dendritic structure shows concentric rings composed of bright discrete elongated spots, a typical character of polycrystalline structure assembled by primary nanoparticles in a highly oriented way. It can be well indexed to crystal planes of face-centred cubic (fcc) structure. The clearly resolved lattice fringes in the HRTEM images were determined as ~0.220 nm, lying between {111}-d-spacing of Pt (0.226 nm) and Ni (0.203 nm). Nanoscale elemental mapping revealed that Pt and Ni were evenly distributed throughout the entire nanodendrite (Figure 1c). Combination with the SAED result, the Pt/Ni alloying nature is obvious. The average molar ratio between Pt and Ni in the dendrites approached Pt: Ni = 3:2 as determined by TEM energy-dispersive X-ray spectroscopy (EDS) data (Pt: Ni = 58.8 : 41.2).

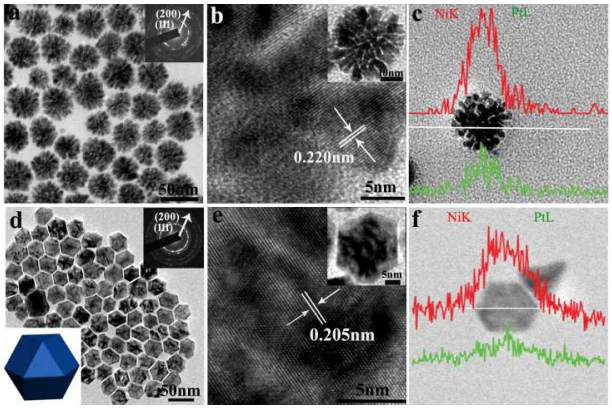

Figure 1. (a, d) survey TEM image, (b, e) HRTEM image, (c, f) elemental mapping profiles of the products obtained at 200 and 220 $^{\circ}C$ for 1 h, respectively. The inserts in Figure 1a and 1d are the corresponding SAED patterns of the nanodendrites and nanocuboctahedrons, respectively.

By elevating the reaction temperature to 220 °C while keeping all other reaction conditions the same, we were able to obtain cubooctahedral nanocrystals. As shown in Figure 1d, the average edge length is *ca.* 35 nm. HRTEM characterization clearly demonstrated the single crystalline structure of an individual cuboctahedron. The adjacent lattice fringe is measured to be 0.205 nm as shown in Figure 1e. The EDS evaluation (Pt/Ni = 20.1: 79.9) revealed the average molar ratio between Pt and Ni is 1: 4. According to Vegard's law, the lattice of a bimetallic alloy would contract with the increasing percentage of the composition of smaller atomic radius. Thus, the observed lattice space difference between the $Pt_{20}Ni_{80}$ cuboctahedrons and the $Pt_{59}Ni_{41}$ dendrites corresponds to the change in composition. The composition-dependent diffraction shift was further confirmed by the corresponding X-ray powder diffraction (XRD) patterns. As can be seen in Figure 2, the diffraction peaks of the $Pt_{59}Ni_{41}$ dendrites moved toward the lower angel region relative to those of the $Pt_{20}Ni_{80}$ cuboctahedrons.

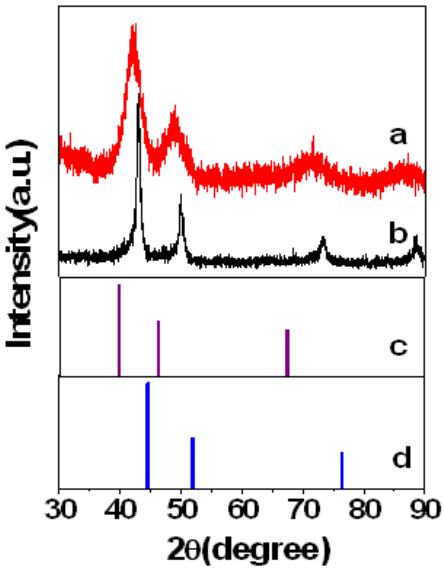

Figure 2. XRD patterns of (a) the $Pt_{59}Ni_{41}$ dendrites, (b) the $Pt_{20}Ni_{80}$ cuboctahedrons, (c) standard Pt with JCPDF No. 04-0802, (d) standard Ni with JCPDF No. 04-0850, respectively.

The quantified crystallographic features regarding the exposed surfaces of the cuboctahedron were proved in detail by TEM observations in combination with the three-dimentional (3-D) modeling as shown in Figure S1. Figure S1a presents the TEM images of the cuboctahedrons with various orientations. As illustrated by the 3-D model (top-right inset of Figure S1a), a cuboctahedron is bounded by six square {100} and eight triangle {111} facets. If the electron beam is aligned to be perpendicular to {001}, the two dimensional (2D) projection is of square shape (Fig. S1c). The truncation along [111] makes the corner parts thinner than the centre part, which accounts for the bright contrast in the four vertex angles of the square (Figure S1b). However, with <111> as the zone axis, the projection exhibits as an equilateral hexagon constructed by the edges of [100] and [110] (Figure S1d and Figure S1e). At the same time, with [110] as the viewing direction, the projection changes into a hexagon (Figure S1g), which is made of two {100} facets and four {111} projections. As indicated in Figure S1f, the angle between the red dashed line and the blue one is 125º, matching well with the crystallographic angle between (111) and (100) facets of the cubic nanostructure (Figure S1g). Clearly, the TEM images matched well with the schematic illustrations of the 3D models of a cuboctahedron.

Since higher temperature is expected to accelerate the nucleation and growth rate of nanoparticles, the temperature-dependent results implied us that morphology evolution from dendrites to cuboctahedron might be kinetically manipulated. To obtain further insight into the growth process, a set of control experiments regarding the reaction time were conducted in detail. TEM observation demonstrated that the products were composed by dendritic nanostructures when the duration was shorter than 1 h at 200 °C (Figure 3a-3c). Although the overall morphology is similar, the size of the branch is quite different. When the duration was elongated from 5 min to 1 h, the branch diameter increased from 2.1~2.7 nm to 3.2~4.6 nm and the length from 6.5~8.0 nm to 8.5~12.5 nm. EDS results revealed that the size increase was accompanied by the composition variation (as shown in Table S1). The Pt/Ni molar ratio of the product collected at 5 min was 88/12, while it decreased to 79/21 after 0.5 h and 59/41 after 1h. After another 30 min reaction, the dendritic structure can no longer be observed while the cuboctahedrons of ~15 nm in diameter dominated the products (Figure 3f). The composition of the cuboctahedrons was determined as $PtNi_2$ with the EDS data of Pt/Ni as 33.03/66.97. Thus, it is apparent that the dendrites involved into the cuboctahedrons accompanied with the increased Ni percentage.

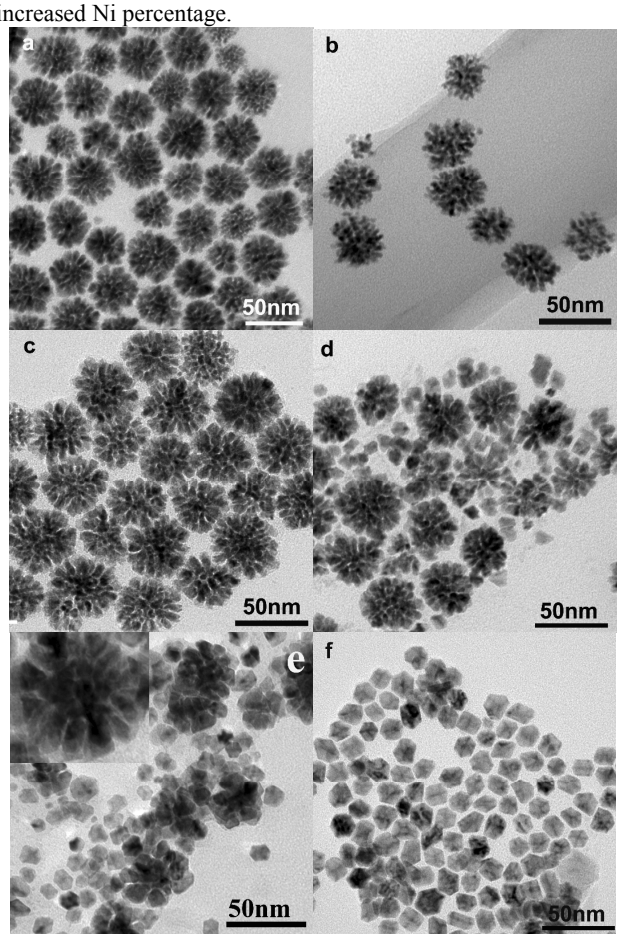

Figure 3. TEM images of the products obtained at 200 °C reacted for different time. (a) 5 min, (b) 30 min, (c) 60 min, (d) 70 min, (e) 80 min, (f) 90 min.

To get further insight into the growth mechanism, we also carried out the control experiments with solely oleylamine (OAm) instead of the mixture of OAm and oleic acid (OA) as the surfactant under conditions similar with those for the products in Figure 3 and Figure 4, respectively. TEM and EDS results reveal that the products were Ni-dominated polyhedrons regardless of the reaction temperature at the initial stage and the Pt proportion increased with the time as shown in Figure S2 and Table S2. Considering that the standard reduction potential for the Ni^{2+}/Ni (E^{θ}= -0.25 eV vs. SHE) is lower than that of $PtCl_6^{2-}/Pt$ (E^{θ} = 0.375 eV vs. SHE), however, $PtCl_6^{2-}$ is easier to reduce than Ni^{2+}. Then, why the Ni-dominated products formed initially? As suggested in Ref. 30, where Cu(II) was reduced before the reduction of Pt(IV), the reduction potential would be changed with the complexation between Pt(IV) and OAm. Recalling the Pt-dominated composition in the presence of OA, we believe the

strong coordination between OA and Ni (II) lowered the reduction potential of Ni(II) efficiently, which led to the retarded reduction of Ni(II) and thus the delayed nucleation of Ni. Thus, when the temperature increased to 200 °C, burst nucleation of Pt occurred as revealed by the observation of the instant precipitation, which produced numerous tiny crystallites. To decrease their total surface energy, these nanocrystallites tended to aggregate into dendritic structures. The presence of OAm was believed helpful for the formation of the 1D Pt-based branch as reported in Lou group's works.[27-29] The coherently extended lattice fringes of the adjacent branches as discussed above indicated that the growth proceeded by the oriented attachment mechanism. Similar growth mechanism was also identified by Xia's group during their preparation of Pt dendritic structures with PVP as the stabilizer.[31] As known as the underpotential deposition (UPD) phenomenon,[15, 32] the noble metal can induce the deposition of non-noble metal ions. Thus, the Pt nuclei catalyzed the generation of Ni atoms by the reduction of Ni^{2+}. The extremely strong alloy tendency promoted the rapidly diffusion of Ni into Pt substrate rather than phase-separated growth,[33,34] which led to both the growing Ni proportion and the increasing size of the branches. TEM observation shows that after 70 min reaction at 200 °C (Figure 3d), isolated nanoparticles of 8~12 nm in diameter appeared besides the dendrites. Prolonging the reaction to 80 min, the isolated nanoparticles with slightly size enlargement dominated the products while the number of the dendritic structures reduced to about 20 percent (Figure 3e). Although the amount of dendritic structure greatly reduced, however, the branch density was still rather high as demonstrated by the more close observation (insert in Figure 3e and Figure S3). The close sizes between the isolated particles and the branches of the dendrites implied us that the increased branch size promoted the dendrites disassembly into separated nanoparticles. The increased strain might be the driving force for the disassembly. After 90 min of reaction, the dendrites eventually disappeared completely, leaving behind the dispersed polyhedral nanoparticles with the average sizes of *ca.* 12 nm (Figure 3f). Although the isolated particles obtained at 70-80 min had irregular shapes, all the final nanocrystals exhibited the specific shape after 90 min of reaction. The gradually size increase and shape focusing suggested that the growth under 200°C agrees well with the classical atomic addition model.

When the reaction temperature was elevated to 220 °C, the growth was obviously accelerated. The dendrites can only stabilize for about 10 min and the time for the complete transformation from the dendrites into the cuboctahedrons were also shortened to 10 min as shown in Figure 4. It is not out of expectation that the growing rate of Ni under 220 °C was faster than that under 200 °C. After 15 min reaction at 220°C, the proportion of Ni is approaching 60%, close to that obtained at 200 °C for 1.5 h (the Ni proportion is 66.97% as described above). The TEM observation revealed that the transformation process from the dendrites to the cuboctahedrons was quite different from that under 200 °C. Figure 4b is the TEM images of the intermediates collected at 220 °C for 15 min. No isolated particles as in Figure 3d and 3e were observed. Instead, the much thicker branches seemed to fuse into each other. It indicated that the branch coalescence and fusion rather than branch disassembly occurred in this case. Thus, it is reasonably to conclude that both atomic addition and particle coalescence had worked during the morphology transformation at 220 °C. The much larger sizes of the cuboctahedrons (~30 nm, Figure 4c) obtained at 220 °C for 30min than those of the same shaped particles (~15 nm) obtained at 200 °C for 90min (Figure 3f) is another evidence for the coalescence process. The penetrated lattice at the grain boundary (as shown in the insert of Figure 4b) revealed that the fusion was completed in an oriented attachment fashion. The growth via the atomic addition was believed worked throughout the reaction. At the initial stage, the atomic addition gave rise to the rapidly enlarged branch size, while it eliminated the blemishes formed during the particle conjugation at the lateral stage.

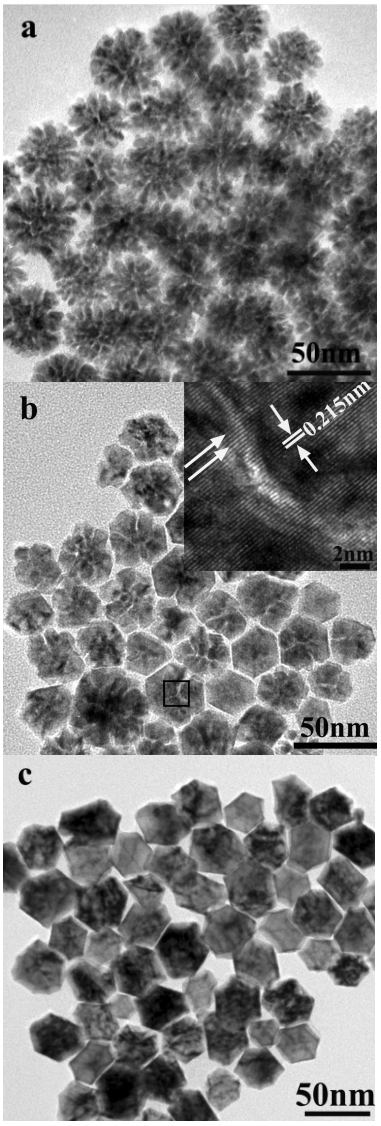

Figure 4. TEM images of the products obtained at 220 °C for different reaction time. (a) 10 min, (b) 15 min, (c) 30 min.

We believe atomic addition and particle mergence were two competitive processes. When the atoms were supplied at a relative low rate, they would have enough time to migrate into the "bulk" of the branches and thus enlarged their sizes. At a high generation rate, the atoms would not only migrate into the bulk

but also diffused at the interfacial region, which resulted in both the branch size increase and the branch coalescence. Furthermore, the sufficient energy supplied by the relative high temperature (220 °C) might meet the energy barrier for the atomic diffusion across the interface of two crystallites and thus also facilitated the particle fusion. The growth process at different temperature is depicted as in scheme 1. Considering the Ni-dominated feature of the polyhedrons obtained either with or without the introduction of OA (Figure 1d, Figure 3f, Figure 4c and Figure S2), we believed the increasing Ni played important roles for the crystal construction from dendrites to nanoparticles in our case. The presumption was further confirmed by the TEM results of the products obtained in the absence of $Ni(acac)_2$ and $PtCl_6^{2-}$. As demonstrated in Figure S4 and S5, without the introduction of $Ni(acac)_2$, the as-prepared pure Pt nanocrystals preferred to exhibit as dendritic morphology, while the pure Ni nanocrystals obtained in the absence of $PtCl_6^{2-}$ mainly assumed irregular polyhedron shapes.

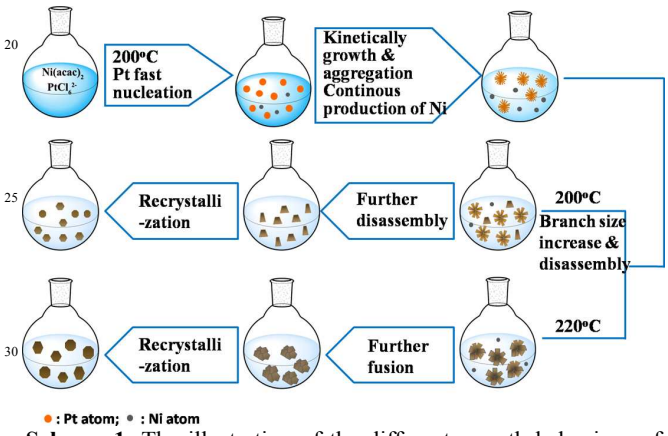

Scheme 1. The illustration of the different growth behaviour of the Pt_xNi_{1-x} nanoalloys under different temperatures.

The electrocatalytic activities of the typical samples including dendritic $Pt_{59}Ni_{41}$ and cubooctahedral $Pt_{33}Ni_{67}$ and $Pt_{20}Ni_{80}$ toward the oxidation of methanol were investigated, which were also benchmarked against the pure Pt nanoparticles (NPs) synthesized under similar conditions but without the introduction of H_2PtCl_6. Figure 5 compares the cyclic voltammetry (CV) curves on the four different catalysts recorded in 0.5 M Ar-saturated H_2SO_4 aqueous solution containing 1.0 M CH_3OH between 0 and 1.0 V at the sweep rate of 50 mV•s^{-1}. During the positive scan, the current increases until a peak is seen at around 0.74 V, which is attributed to the electro-oxidation of methanol. When the potential scan is reversed, a peak centred at 0.56 V occurs, which is due to the reactivation of Pt-oxides. As shown in Figure 5a, the area-normalized specific peak current densities associated with methanol oxidation in the forward scan for the dendritic $Pt_{59}Ni_{41}$, cubooctahedral $Pt_{33}Ni_{67}$, $Pt_{20}Ni_{80}$ and pure Pt were 10.3, 6.5, 3.6 and 3.3 A•m^{-2}, respectively. That is, the dendritic nanostructures had a specific activity of 1.6 times that of the cubooctahedral $Pt_{33}Ni_{67}$ and 2.8 times that of the cubooctahedral $Pt_{20}Ni_{80}$ and pure Pt nanocrystals.

The durability of electrocatalytic materials has been recognized as one of the most important issues to be addressed before the commercialization of DMFCs. To evaluate the electrochemical stabilities of catalysts, chronoamperometric measurements for the MOR were performed in 0.5 M CH_3OH + 1.0 M H_2SO_4 at 0.70 V. As seen from Figure 5b, the current densities of all catalysts decay rapidly at the initial stage, which may be due to hydrogen adsorption, the double-layer discharge, and the formation of intermediate species during methanol oxidation such as CO_{ads} and CHO_{ads}.[35-37] After several minutes, the current subsequently decreased slowly and a pseudo-steady state is achieved for the catalysts. The methanol oxidation currents on dendritic $Pt_{59}Ni_{41}$, cubooctahedral $Pt_{33}Ni_{67}$, $Pt_{20}Ni_{80}$ and pure Pt are 3.8, 0.73 and 0.38, 0.40 A•m^{-2} at 600 s, indicating that the CO-like intermediates tolerance of the dendritic $Pt_{59}Ni_{41}$ is much better than those of the cuboctahedrons. To further compare the CO tolerant ability, the long-term poisoning rate (δ) is calculated by measuring the linear decay of the current according to the following equation[38,39]:

$$\delta(\%s^{-1}) = \frac{100}{I_0} \times \left(\frac{dI}{dt}\right)_{t>500s}$$

where $(dI/dt)_{t>500s}$ is the slope of the linear portion of the current decay, and I_0 is the current at the start of polarization back extrapolated from the linear current decay. The poisoning rate was calculated as 0.04%, 0.07%, 0.08% and 0.09% s^{-1} for the dendritic $Pt_{59}Ni_{41}$, cubooctahedral $Pt_{33}Ni_{67}$, $Pt_{20}Ni_{80}$ and pure Pt, respectively. Obviously, the $Pt_{59}Ni_{41}$ dendrites possessed the lower poisoning rate and thus the higher tolerance to intermediate species formed during the MOR.

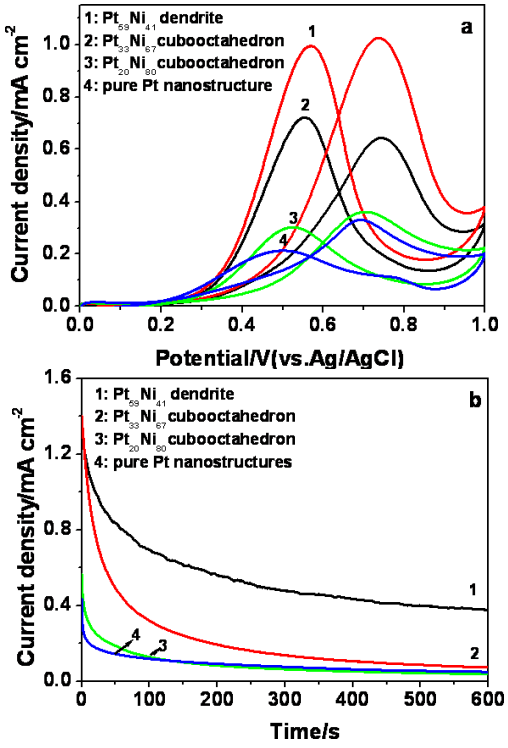

Figure 5 Cyclic voltammograms of Pt-Ni nanoalloys in (a) 0.5 mol/L H_2SO_4 + 1.0 mol/L CH_3OH, (b) Chronoamperometry curves of Pt-Ni nanohybrids in 0.5 mol/L H_2SO_4 + 1.0 mol/L CH_3OH at 0.7 V. The scanning rate in all cases is 50 mV/s.

It was believed that the catalytic performance of Pt-based catalysts has closely relation with the d-band position, which can be tuned by the addition of 3d transition metal.[10-15,40,41] To learn

more about the catalytic performance difference, XPS characterization was employed to determine the interaction between Pt and Ni atoms. Curves 1 to 3 in Figures 5 are the corresponding XPS spectra of Pt 4f core-level in dendritic $Pt_{59}Ni_{41}$ and cubooctahedral $Pt_{33}Ni_{67}$ and $Pt_{20}Ni_{80}$, respectively. It reveals that the Pt 4f signal of both cubooctahedral structures is composed by two peaks for metallic Pt (0), located at 70.9, 74.8 eV for $Pt_{33}Ni_{67}$ and 71.06, 74.43 eV for $Pt_{20}Ni_{80}$, respectively. For the $Pt_{59}Ni_{41}$ dendrites, the Pt 4f can be deconvoluted into two components, two strong peaks located at 71.06, 74.8eV and two weak ones at 74.3, 78.4 eV, respectively. The former pair is the characteristic peaks for metallic Pt (0), while the latter can be assigned to the $Pt^{IV}O_2$ species, respectively.[35] In comparison with the data of pure Pt (71.32 eV),[42] the binding energy values of Pt (0) species negatively shifted 0.42 eV for $Pt_{33}Ni_{67}$ cuboctahedrons and 0.26 eV for $Pt_{59}Ni_{41}$ dendrites and $Pt_{20}Ni_{80}$ cuboctahedrons, respectively.

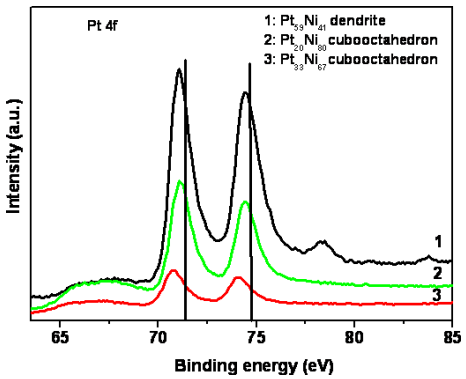

Figure 6 The XPS spectra of Pt 4f core level for the products with different composition and morphology. (1) $Pt_{59}Ni_{41}$ dendrites, (2) $Pt_{20}Ni_{80}$ cuboctahedrons, (3) $Pt_{33}Ni_{67}$ cuboctahedrons. The vertical line indicates the peak position of pure Pt nanoparticles.

The contribution from the modified electronic structure for the improved catalytic activity was further confirmed by the measurements with the physical mixture of Pt and Ni nanoparticles as the catalysts. As shown in Figure S6 in the supplementary information, the area-normalized specific peak current densities associated with methanol oxidation in the forward scan for the mixture with Pt/Ni ratios as 3/2, 1/2 and 1/4 were 2.0, 0.9 and 0.4 $A•m^{-2}$, respectively, which were much lower than the data of pure Pt (3.3 $A•m^{-2}$), not mention those for the nanoalloys.

In conjunction with the electrochemical data, it indicated that the morphology is also an important parameter determining the catalytic activities. The enhanced performance of the dendrites could be ascribed to the following reasons: 1) the presence of more edges and corners as well as high-index facets on the branches of the dendrites may provide more active sites for MOR; 2) the interconnected 3D structure of the dendrites might make the nanostructures more stable and thus the enhanced durability.[43-45] However, for the products with similar shapes (cubooctahedral $Pt_{33}Ni_{67}$ and $Pt_{20}Ni_{80}$), the d-band position seems determining the catalytic activity. The lower the d-band position is (70.9 eV for $Pt_{33}Ni_{67}$ cuboctahedrons and 71.06 eV for $Pt_{20}Ni_{80}$ cuboctahedrons), the higher the catalytic activity is.

Conclusions

In summary, we achieved the composition and morphology control of Pt_xNi_{1-x} ($0 < x < 1$) nanoalloys by simply adjusting the reaction temperature and/or duration time. TEM observations combined with EDS characterization indicate that the Ni-rich cuboctahedrons were evolved from the Pt-rich dendrites. However, the growth behaviour was different under different temperature. At 200 °C, the atomic addition played key role for the morphology and composition transformation, while both atomic addition and oriented attachment had worked under 220 °C. The methanol oxidation reaction was chosen as the model reaction to investigate the electrocatalytic performance of the typical samples with different composition and morphology. The dendrites exhibited the higher catalytic activity and better durability relative to the cuboctahedrons. For the cuboctahedrons with different composition, the catalytic activity is mainly determined by the d-band position.

Notes and references

Key Laboratory of Bio-inspired Smart Interfacial Science and Technology of Ministry of Education, Beijing Key Laboratory of Bio-inspired Energy Materials and Devices, School of Chemistry and Environment, Beihang University, Beijing 100191, PR China. Fax: 861082338492; Tel: 861082338492; E-mail: dfzhang@buaa.edu.cn; guolin@buaa.edu.cn

† Electronic Supplementary Information (ESI) available: [The TEM and 3D modeling of the detailed crystallographic features of the $Pt_{20}Ni_{80}$ polyhedrons, the composition data of the samples collected at different duration time under different temperature]. See DOI: 10.1039/b000000x/

Acknowledgment

The project was supported by National Natural Science Foundation of China (21173015), the National Key Basic Research Program of China (973) (2010CB934700).

1 S. Mukerjee, S. Srinivasan, M. P. Soriaga and J. Mcbreen, *J. Phys. Chem.* 1995, **99**, 4577.
2 J. Greeley and M. Mavrikakis, *Nat. Mater.* 2004, **3**, 810.
3 Z. M. Peng and H. Yang, *Nano Today* 2009, **4**, 143.
4 C. Chen and P. Holt-Hindle, *Chem. Rev.* 2010, **110**, 3767.
5 V. R. Stamenkovic, B. Fowler, B. S. Mun, G. F. Wang, P. N. Ross, C. A. Lucas and N. M. Markovic, *Science* 2007, **315**, 493.
6 J. Nøskov, F. Abild-Pedersen, F. Studt and T. Bligaard, *Proc. Natl. Acad. Sci. U. S. A.* 2011, **108**, 937.
7 H. Zhang, M. S. Jin and Y. N. Xia, *Chem. Soc. Rev.* 2012, **41**, 8035.
8 S. Alayoglu, A. U. Nilekar, M. Mavrikakis and B. Eichhorn, *Nat. Mater.* 2008, **7**, 333.
9 U. Nilekar, S. Alayoglu, B. Eichhorn and M. Mavrikakis, *J. Am.Chem. Soc.* 2010, **132**, 7418.
10 Y. Xu, A. V. Ruban and M. Mavrikakis, *J. Am. Chem. Soc.* 2004, **126**, 4717.
11 J. Knudsen, A. U. Nilekar, R. T. Vang, J. Schnadt, E. L. Kunkes, J. A. Dumesic, M. Mavrikakis and F. Besenbacher, *J. Am. Chem. Soc.* 2007, **129**, 6485.
12 H. Y. Su, X. H. Bao and W. X. Li, *J. Chem. Phys.* 2008, **128**, 194707.
13 J. R. Kitchin, J. K. Norskov, M. A. Barteau and J. G. Chen, *J. Chem. Phys.* 2004, **120**, 10240.
14 P. Strasser, S. Koh, T. Anniyev, J. Greeley, K. More, C. Yu, Z. Liu, S. Kaya, D. Nordlund, H. Ogasawara, M. F. Toney and A. Nilsson, *Nat. Chem.* **2010**, **2**, 454.
15 J. Gu, Y. W. Zhang and F. Tao, *Chem. Soc. Rev.* 2012, **41**, 8050.

16 H. Chen, D. L. Wang, Y. C. Yu, K. A. Newton, D. A. Muller, H. Abruña and F. J. DiSalvo, *J. Am. Chem. Soc.* 2012, **134**, 18453.

17 M. K. Carpenter, T. E. Moylan, R. S. Kukreja, M. H. Atwan and M. M. Tessema, *J. Am. Chem. Soc.* 2012, **134**, 8535.

18 C. H. Cui, L. Gan, H. H. Li, S. H. Yu, M. Heggen and P. Strasser, *Nano Lett.* 2012, **12**, 5885.

19 J. B. Wu, L. Qi, H. J. You, A. Gross, J. Li and H. Yang, *J. Am. Chem. Soc.* 2012, **134**, 11880.

20 C. Wang, M. F. Chi, G. F. Wang , D. van der Vliet, D. G. Li, K. More, H. H. Wang, J. A. Schlueter, N. M. Markovic and V. R. Stamenkovic, *Adv. Funct. Mater.* 2011, **21**, 147.

21 X. Q. Huang, E. B. Zhu, Y. Chen, Y. J. Li, C. Y. Chiu, Y. X. Xu, Z. Y. Lin, X. F. Duan and Y. Huang, *Adv. Mater.* 2013, **25**, 2974.

22 Y. Wu, S. F. Cai, D. S. Wang, W.He and Y. D. Li, *J. Am. Chem. Soc.* 2012, **134**, 8975.

23 J. Zhang, H. Yang, J. Fang and S. Zou, *Nano Lett.* 2010, **10**, 638

24 J. B. Wu, A. Gross and H. Yang, *Nano Lett.* 2011, **11**, 798.

25 J. Wu, J. Zhang, Z. Peng, S. Yang, F. T. Wagner and H. Yang, *J. Am. Chem. Soc.* 2010, **132**, 4984.

26 Y. Wu, S. Cai, D. Wang, W. He and Y. Li, *J. Am. Chem. Soc.* 2012, **134**, 8975.

27 B. Y. Xia, H. B. Wu, X. Wang and X. W. (David) Lou, *Angew. Chem. Int. Ed.* 2013, **52**, 12337.

28 B. Y. Xia, W. T. Ng, H. B. Wu, X. Wang and X. W. (David) Lou, *Angew. Chem. Int. Ed.* 2012, **51**, 7213.

29 B. Y. Xia, H. B. Wu, Y. Yan, X. W. (David) Lou and X. Wang, *J. Am. Chem. Soc.* 2013, **135**, 9480.

30 B. Y. Xia, H. B. Wu, X. Wang and X. W. (David) Lou, *J. Am. Chem. Soc.* 2012, 134, 13934.

31 B. Lim, M. Jiang, T. Yu, P. H. C. Camargo and Y. Xia, *Nano Res.* 2010, **3**, 69.

32 E. Herrero, L. J. Buller and H. D. Abruna, *Chem. Rev.* 2001, **101**, 1897.

33 J. Zhang, H. Z. Yang, J. Y. Fang and S. Z. Zou, *Nano Lett.* 2010, **10**, 638.

34 T. C. Deivaraj, W. X. Chen and J. Y. Lee, *J. Mater. Chem.* 2003, **13**, 2555

35 J. F. Xu, X. Y. Liu, Y. Chen, Y. M. Zhou, T. H. Lu and Y. W. Tang, *J. Mater. Chem.* 2012, **22**, 23659.

36 G. Zhang, Y. Wang, X. Wang, Y. Chen, Y. Zhou, Y. Tang, L. Lu, J. Bao and T. Lu, *Appl. Catal., B* 2011, **102**, 614.

37 Kabbabi, R. Faure, R. Durand, B. Beden, F. Hahn, J. M. Leger and C. Lamy, *J. Electroanal. Chem.* 1998, **444**, 41.

38 J. Guo, T. Zhao, J. Prabhuram, R. Chen and C. Wong, *Electrochim Acta* 2005, **51**, 754.

39 J. F. Xu, X. Y. Liu, Y. Chen, Y. M. Zhou, T. H. Lu and Y. W. Tang *J. Mater. Chem.* 2012, **22**, 23659.

40 P. Strasser, S. Koh, T. Anniyev, J. Greeley, K. More, C. Yu, Z. Liu, S. Kaya, D. Nordlund, H. Ogasawara, M. F. Toney and A. Nilsson, *Nat. Chem*. 2010, **2**, 454.

41 X. M. Wang, Y. Orikasa, Y. Takesue, Hi. Inoue, M. Nakamura, T. Minato, N.Hoshi and Y. Uchimoto, *J. Am. Chem. Soc.* 2013, **135**, 5938.

42 S. G. Chen, Z. D. Wei, X. Q. Qi, L. C. Dong, Y. G. Guo, L. J. Wan, Z. G. Shao and L. Li, *J. Am. Chem. Soc.* 2012, **134**, 13252.

43 M. A. Mahmoud, C. E. Tabor, M. A. El-Sayed, Y. Ding and Z. L. Wang, *J. Am. Chem. Soc.* 2008, **130**, 4590.

44 H. Lee, S. E. Habas, S. Kweskin, D. Butcher, G. A. Somorjai and P. D. Yang, *Angew. Chem. Int. Edit.* 2006, **45**, 7824.

45 T. K. Sau and A. L. Rogach, *Adv. Mater.* 2010, **22**, 1781.